Ideal superelasticity in Ni-based Heusler alloys

Peiyu Cao [a,b], Fuyang Tian [c,*], Wei Li [d], Levente Vitos [d,e,f], Yandong Wang [a,*]

[a] Beijing Advanced Innovation Center for Materials Genome Engineering, State Key Laboratory for Advanced Metals and Materials, University of Science and Technology Beijing, Beijing 100083, China
[b] State Key Laboratory of Nonlinear Mechanics, Institute of Mechanics, Chinese Academy of Sciences, Beijing 100190, China
[c] Institute for Applied Physics, University of Science and Technology Beijing, Beijing 100083, China
[d] Applied Materials Physics, Department of Materials Science and Engineering, Royal Institute of Technology, Stockholm SE-100 44, Sweden
[e] Department of Physics and Astronomy, Division of Materials Theory, Uppsala University, Uppsala SE-75120, Sweden
[f] Wigner Research Centre for Physics, Institute for Solid State Physics and Optics, Budapest H-1525, Hungary

ARTICLE INFO

ABSTRACT

The hysteresis that occurs during superelasticity caused by the stress-induced first-order martensite transformation is sometimes detrimental to the properties of superelastic materials. In this paper, first-principles calculations are performed to systematically investigate the effects of the chemical composition and crystal disorder on the superelasticity of $Ni_{50-x}Co_xM_{25}Ga_{25}$ (M = Mn, Fe) Heusler alloys. Calculations of the stress-strain relation in the studied alloys reproduce the recent experimental findings for nonhysteretic superelasticity within an acceptable range of composition and ordering. We evaluate the Bloch spectral function to study the Fermi surface topology in connection with nonhysteretic superelasticity. We propose the Landau-de Gennes model-dependent critical parameter P_c, which can be used to predict the composition range of nonhysteretic superelastic materials. For the ferromagnetic $L2_1$ $Ni_{50-x}Co_xMn_{25}Ga_{25}$ and B2 $Ni_{50-x}Co_xFe_{25}Ga_{25}$ alloys, the nonhysteretic superelasticity phenomenon theoretically occurs for Co contents over $x = 16$ at.% and $x = 28$ at.%, respectively.

1. Introduction

Based on the well-known Frenkel theory [1], the elasticity and strength limits in crystal solids are approximately 1/10 and $\mu/10$, respectively, where μ is the shear modulus along a specific crystal direction. The upper limits of elasticity and strength are of obvious interest for the study of strong solid materials with high elasticity; however, most crystal materials have elasticity limits that fall within 1%, except for certain nanowires that approach the ideal elastic strain limit (~ 16%) [2]. In addition to simple elasticity, an alternative recoverable type of strain in materials, that could break such limits involves pseudoelasticity or superelasticity that is associated with reversible stress-induced structural phase transformations, such as martensitic transformations (MTs) in ferroelastic alloys. Under the action of an external force, certain shape memory alloys (SMAs) have a much greater deformation recovery ability than traditional metals and alloys [3]; that is, the large strain generated during loading can be recovered after unloading. This property is widely used in the biomedical field, architectural shock absorption, and daily life. For example, eyeglass frames made of

SMAs can withstand a much larger deformation than normal materials without damage [4]. The physical nature of superelasticity is that stress induces martensitic transformation during stress loading, and its reverse transformation occurs during stress unloading, which also results in hysteresis during loading and unloading. This hysteresis has a key impact on the recoverability of SMAs and consumes mechanical energy [5,6]. In addition, it causes an additional uncertainty in the application of SMAs detrimental to the precise control of devices.

Kosogor et al. observed a nonhysteretic superelasticity in a Ni-Fe(Co)-Ga single-crystal alloy when the temperature exceeded the critical value of 320 K, whereas hysteresis occurred again below this temperature [7]. However, it is impractical to eliminate hysteresis by controlling the temperature due to various environmental conditions. Through transmission electron microscopy (TEM), Waitz et al. found that the martensitic transformation of Ni-Ti alloys was completely suppressed with a decrease in the grain size (the critical size was approximately 60 nm) [8-10]. Recently, Liu et al. reported that the shape memory effect of bent Cu-Al-Ni nanopillars diminished (from 350 to 130 nm) and even disappeared (when the diameter was smaller than 130 nm) as the sample diameter decreased. This was due to the complex stacking sequences that dominated the original twinning and suppressed the

phase transformation [11,12]. A similar size effect occurs in other nanosized SMAs, such as Au-Cd [13] and Fe-Pd [14] alloys. However, due to the limitation of the size effect, this method can only be applied to low-dimensional (nanometer) materials, and it is difficult to eliminate the hysteresis in high-dimensional (bulk) materials.

Recently, an "ideal" nonhysteretic superelasticity was observed in Ni-Co-Fe-Ga alloys [15]. Chen *et al.* reported a large nonhysteretic superelasticity of up to 15.2% in $Ni_{35}Co_{20}Fe_{18}Ga_{27}$ single crystals that exhibited a small temperature dependence and high energy storage capability. However, the experimental results are still not fully understood. In order to further reveal the physical nature of the non-hysteretic superelasticity phenomenon and to design high-performance materials more efficiently, in this paper, we attempt to obtain nonhysteretic superelasticity by adjusting the composition (increasing Co content to replace Ni) and disorder (constructing $L2_1$, B2 and A2 structures) of Ni(Co)-M-Ga (M = Mn, Fe) alloys. The crystallographic information and atom occupancy will be described in detail in Section 2.

Ni-Mn-Ga alloys are one of the earliest and most investigated ferromagnetic shape memory alloys (FSMAs) among Heusler alloys. These alloys have a two-way shape memory effect [16,17], superelasticity [18] and magnetostriction effect [19,20]. Research on Ni-Fe-Ga alloys began with the doping of Ni_2MnGa with Fe. Oikawa *et al.* first reported ternary Ni-Fe-Ga alloys in 2002 [21]. Compared with that of Ni-Mn-Ga alloys, the ductility of Ni-Fe-Ga alloys has been greatly improved, which is conducive to their practical application. For both Ni-Mn-Ga and Ni-Fe-Ga alloys, the addition of Co improves the extent of magnetostriction [22,23] and superelasticity [24,25].

In this paper, the effects of Co element content and disorder on mechanical behaviors (especially the nonhysteretic superelasticity) of ferromagnetic (FM) and antiferromagnetic (AFM) $Ni_{50-x}Co_xM_{25}Ga_{25}$ (M = Mn, Fe) Heusler alloys were investigated by first-principles calculations based on the exact muffin-tin orbital (EMTO) method [26-28] in combination with the coherent potential approximation (CPA) [29-33].

2. Computational details

For $Ni_{50-x}Co_xM_{25}Ga_{25}$ (M = Mn, Fe) Heusler alloys, the most common Strukturbericht crystal structure is $L2_1$ with the space group $Fm\bar{3}m$ (No. 225). In addition, B2 ($Pm\bar{3}m$, No. 221) and A2 ($Im\bar{3}m$, No. 229) crystal structures were also found in these alloys [34,35], especially at high temperatures [36,37]. To facilitate a direct comparison among different crystal structures, we uniformly constructed a cube supercell of 16 atoms, which can be considered a $2 \times 2 \times 2$ body-centered cubic (bcc) lattice. The three structures are all shown in Fig. 1. For three structures ($L2_1$, B2, and A2), ferromagnetism (FM) is the most likely stable magnetic state. In particular, the antiferromagnetism (AFM) of the B2 structure is also considered. Our initial calculations tests showed that, with uniaxial tension along <001> direction, the $Ni_{50-x}Co_xM_{25}Ga_{25}$ (M = Mn, Fe) alloys undergo tetragonal deformation instead of orthogonal deformation, which is consistent with our previous experiments [15]. The tetragonal deformation along the Bain path can be described in the form of a matrix

$$D_t + I = \begin{pmatrix} 1+\delta_{t1} & 0 & 0 \\ 0 & 1+\delta_{t1} & 0 \\ 0 & 0 & 1+\delta_{t2} \end{pmatrix}, \quad (1)$$

where D_t is the stain matrix of tetragonal deformation; I is the 3×3 identity matrix; $\delta_{t1} = \frac{a-a_0}{a_0}$ and $\delta_{t2} = \frac{c-a_0}{a_0}$ are both tetragonal deformation parameter (for uniaxial tensile state $\delta_{t1} < 0$ and $\delta_{t2} > 0$). After tetragonal deformation, it is possible to form a stable unmodulated martensitic structure, whose space group is $I4/mmm$

(No. 139) for $L2_1$ and A2 structures, and $P4/mmm$ (No. 123) for B2 structure.

In the present calculations, the framework of the EMTO-CPA was carried out for the description of chemical disorder. The Perdew-Burke-Ernzerhof (PBE) generalized gradient approximation (GGA) [38] was adopted to describe the exchange-correlation potential. Soft-core approximations and scalar relativistics were employed. The k-point mesh was set to $13 \times 13 \times 13$ for all 16 atomic cube supercells. The convergence criterion of total energy was set as 10^{-7} Ry. The basis sets for the EMTO included s, p, d, and f orbitals. Ni $3d^8 4s^2$, Mn $3d^5 4s^2$, Fe $3d^7 4s^1$, Ga $3d^{10} 4s^2 4p^1$, and Co $3d^7 4s^2$ were treated as valence states. In addition to cubic crystals, the EMTO method can accurately calculate the total energy of anisotropic crystals, such as a tetragonal crystal structure. In the present research, each volume was relaxed for all cubic and tetragonal crystal structures to obtain the most stable energy.

3. Results and discussion

3.1. Equilibrium state

Table 1 lists the equilibrium lattice constants, elastic moduli, and magnetic moments of the stoichiometric $Ni_{50}Mn_{25}Ga_{25}$ and $Ni_{50}Fe_{25}Ga_{25}$ Heusler alloys in comparison with the experimental values and previous theoretical results to assess the accuracy of our first-principles method. For the $Ni_{50}Mn_{25}Ga_{25}$ ($Ni_{50}Fe_{25}Ga_{25}$) Heusler alloy in the $L2_1$ (FM) austenitic phase, our calculated lattice constant of $a = 5.8140$ Å ($a = 5.7712$ Å) is consistent with the experimental values and previous calculations ranging from 5.774 Å (5.74 Å) to 5.8368 Å (5.77 Å), except for the 5.65 Å of the $Ni_{50}Mn_{25}Ga_{25}$ austenitic phase calculated by Rached *et al.* Their calculated results were obtained by using the full-potential linear muffin-tin orbital (FP-LMTO) method [39,40] within the local spin-density approximation (LSDA) [41]. Compared with the generalized gradient approximation (GGA), the local density approximation (LDA) and LSDA tend to underestimate the lattice constant a and overestimate the bulk modulus B. This is due to the relatively simple modification of the exchange and correlation energy part, which does not describe the $3d$ electronic charge density well [42]. Our calculated bulk modulus $B = 154.7$ GPa ($B = 160.6$ GPa) is consistent with the experimental values and previous calculation results ranging from 146 GPa (145.6 GPa) to 157.3 GPa (170.0 GPa), except for the 206.5 GPa for the $Ni_{50}Mn_{25}Ga_{25}$ austenitic phase calculated by Rached *et al.* and 107 GPa measured by Mañosa *et al.* The tetragonal shear modulus $c' = 22$ GPa may be overestimated by Mañosa *et al.* and the elastic constant $c_{44} = 39.6$ GPa may be underestimated by Rached *et al.* For the $Ni_{50}Mn_{25}Ga_{25}$ ($Ni_{50}Fe_{25}Ga_{25}$) Heusler alloy with the $L2_1$ (FM) unmodulated martensitic phase, our calculated lattice constants a, c, c/a, and bulk modulus B are consistent with the available theoretical results. However, the experimental lattice constants are smaller than the calculation results, which may be caused by the modulation and off-stoichiometry composition. The total and local magnetic moments of stoichiometric $Ni_{50}Mn_{25}Ga_{25}$ and $Ni_{50}Fe_{25}Ga_{25}$ Heusler alloys are also listed in Table 1. For $Ni_{50}Mn_{25}Ga_{25}$ with the $L2_1$ (FM) austenitic phase, the total magnetic moment $\mu_{tot} = 4.066$ μ_B is consistent with the experimental value of 4.17 μ_B and previous calculation results ranging from 3.73 μ_B to 4.27 μ_B. In the absence of experimental and calculated values, the total magnetic moment of martensite $\mu_{tot} = 4.147$ μ_B is slightly higher than that of austenite. The increase in the total magnetic moment mainly comes from the local magnetic moment contribution of the Ni atom. For $Ni_{50}Fe_{25}Ga_{25}$ with the $L2_1$ (FM) austenitic phase, the total magnetic moment $\mu_{tot} = 3.455$ μ_B is consistent with previous calculation results ranging from 3.126 μ_B to 3.41 μ_B. However, all calculation results are slightly higher than the experimental val-
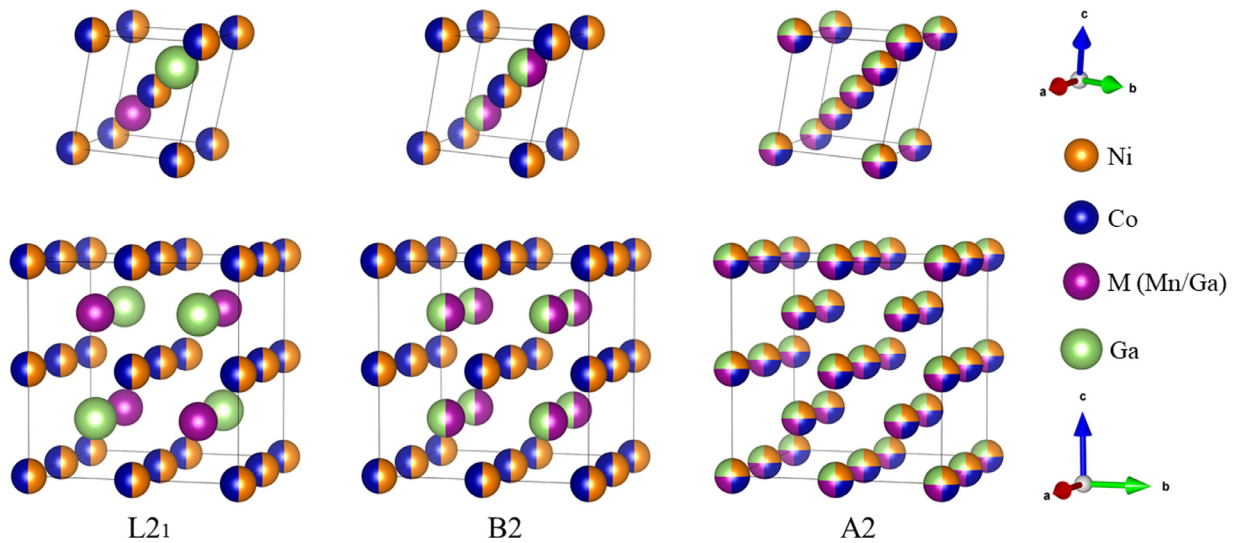
Fig. 1. The 16 atomic crystal cells of three structures (L2$_1$, B2, and A2), and their corresponding 4 atomic primitive cells.

Table 1
The equilibrium lattice constants a (Å), c (Å), and c/a, bulk modulus B (GPa), tetragonal shear modulus c' (GPa), elastic content c_{44} (GPa), and total and local magnetic moments μ (μ_B) for the Ni$_{50}$Mn$_{25}$Ga$_{25}$ and Ni$_{50}$Fe$_{25}$Ga$_{25}$ Heusler alloys in the L2$_1$ (FM) austenitic and corresponding unmodulated martensitic phases, respectively. Experimental values and previous calculations are also listed for comparison.

Alloy	Method	Lattice parameter				Elastic modulus				Magnetic moment				
		a	c	c/a	Ref.	B	c'	c_{44}	Ref.	μ_{tot}	μ_{Ni}	$\mu_{Mn/Fe}$	μ_{Ga}	Ref.
Ni$_{50}$Mn$_{25}$Ga$_{25}$	Our Cal.	5.8140	5.8140	1.000		154.7	8.0	127.0		4.066	0.308	3.520	-0.070	
(Austenite)	Exp.	5.8250	5.8250	1.000	[43]	146	4.5	103	[44]	4.17	0.33	3.86	–	[43]
		5.823	5.823	1.000	[45]	107	22	102	[46]					
	Other Cal.	5.8127	5.8127	1.000	[37]	157.3	7.2	107.1	[37]	3.96	0.29	3.45	-0.07	[37]
		5.65	5.65	1.000	[47]	206.5	5.7	39.6	[47]	3.73	0.315	3.10	-0.041	[47]
		5.8368	5.8368	1.000	[48]	155	2.5	100	[48]	4.27	–	–	–	[48]
		5.8104	5.8104	1.000	[49]	156	–	–	[49]	4.09	0.37	3.36	-0.04	[49]
		5.8226	5.8226	1.000	[50]	156.7	7.5	113.4	[50]	3.98	–	–	–	[50]
		5.805	5.805	1.000	[51]	151	–	–	[51]	4.20	0.35	3.52	-0.06	[51]
		5.774	5.774	1.000	[51]					4.23	0.33	3.61	-0.028	[52]
		5.805	5.805	1.000	[53]					4.224	–	–	–	[53]
Ni$_{50}$Mn$_{25}$Ga$_{25}$	Our Cal.	5.3736	6.7868	1.263		155.2				4.147	0.341	3.531	-0.066	
(Martensite)	Exp.	–	–	1.18	[54]									
	Other Cal.	–	–	1.25	[50]									
		–	–	1.26	[55]									
		–	–	1.27	[56]									
Ni$_{50}$Fe$_{25}$Ga$_{25}$	Our Cal.	5.7712	5.7712	1.000		160.6	-3.4	124.5		3.455	0.281	2.937	-0.045	
(Austenite)	Exp.	5.7405	5.7405	1.000	[57]					3.035	–	–	–	[58]
		5.76	5.76	1.000	[59]									
		5.74	5.74	1.000	[60]									
		5.75	5.75	1.000	[61]	145.6	–	–	[61]					
	Other Cal.	5.752	5.752	1.000	[51]	164	–	–	[51]	3.41	0.28	2.91	-0.04	[51]
		5.755	5.755	1.000	[62]					3.126	0.237	2.673	-0.021	[58]
		5.76	5.76	1.000	[63]	165.1	–	–	[63]	3.29	0.25	2.82	-0.04	[63]
		5.77	5.77	1.000	[52]	170.0	–	–	[52]	3.25	-0.05	2.82	-0.026	[52]
		5.77	5.77	1.000	[64]	164.4	–	–	[64]	3.31	0.29	2.87	–	[64]
Ni$_{50}$Fe$_{25}$Ga$_{25}$	Our Cal.	5.2064	7.0338	1.351		160.2				3.434	0.278	2.927	-0.048	
(Martensite)	Exp.	4.62	5.38	1.17	[59]									
	Other Cal.	5.22	6.94	1.33	[63]	165.8	–	—	[63]	3.31	0.34	2.69	-0.06	[63]
		5.24	6.97	1.33	[64]					3.36	0.37	2.75	–	[64]
		–	–	1.35	[52]					3.31	0.37	2.67	-0.03	[52]

ues. The total magnetic moment of martensite $\mu_{tot} = 3.434$ μ_B is almost equal to that of austenite, including the local magnetic moment of each element. As shown in Table 1, our calculated results are in good agreement with the experimental values and theoretical results.

The lattice constants of the Ni$_{50-x}$Co$_x$Mn$_{25}$Ga$_{25}$ and Ni$_{50-x}$Co$_x$Fe$_{25}$Ga$_{25}$ alloys are shown in Fig. 2. For the L2$_1$ (FM) austenitic Ni$_{50-x}$Co$_x$Mn$_{25}$Ga$_{25}$ alloys, as shown in Fig. 2a, our calcu-

lated lattice constants are in good agreement with the calculation results based on the Vienna *ab initio* software package (VASP) by Bai *et al.* [53] and X-ray diffraction (XRD) experimental results at room temperature by Kanomata *et al* [65]. Fig. 2a and b shows that the lattice constants decrease monotonically with increasing Co content for all structures. This may be because the ionic radius of Co is slightly smaller than that of Ni when Co atoms replace Ni. For both the Ni$_{50-x}$Co$_x$Mn$_{25}$Ga$_{25}$ and Ni$_{50-x}$Co$_x$Fe$_{25}$Ga$_{25}$ alloys, the
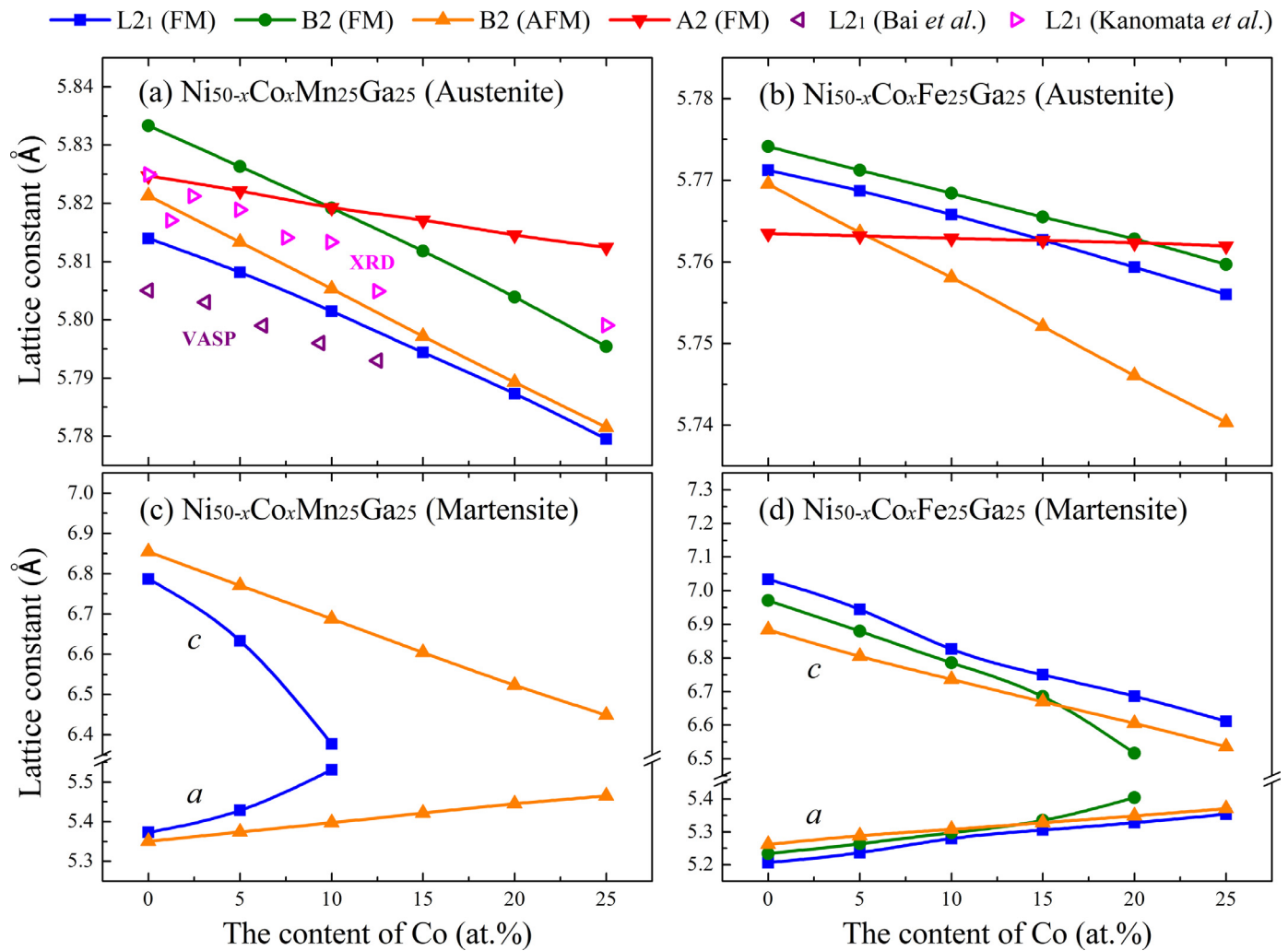
Fig. 2. The lattice constants of the $Ni_{50-x}Co_xMn_{25}Ga_{25}$ (left) and $Ni_{50-x}Co_xFe_{25}Ga_{25}$ (right) alloys as a function of Co content (at.%) for the $L2_1$ (FM), B2 (FM), B2 (AFM), and A2 (FM) cubic austenite (top) and corresponding unmodulated tetragonal martensite (bottom) phases.

rate of lattice constant decline in A2 (FM) is significantly lower than that in the three other structures due to the different solid solution mechanisms of Ni and Co elements. For the A2 structure, Ni and Co elements occupy all the lattice points uniformly. For the B2 and $L2_1$ structures, Ni and Co occupy only half of these lattice sites. Fig. 2c and d shows the lattice constants of the corresponding unmodulated tetragonal martensite phases. For both $Ni_{50-x}Co_xMn_{25}Ga_{25}$ and $Ni_{50-x}Co_xFe_{25}Ga_{25}$ alloys, the lattice constant a increases, and c decreases with an increase in Co content; thus, this leads to a monotonic decrease in c/a.

3.2. Energy variation and stability

Fig. 3 shows the total energy (ΔE) as a function of strain (ε) for the tetragonal distortion along the Bain path. Compared with that for the other three structures, the ΔE of $L2_1$ (FM) has a minimum value throughout the entire Bain path for $Ni_{50-x}Co_xMn_{25}Ga_{25}$ and $Ni_{50-x}Co_xFe_{25}Ga_{25}$ alloys. Similarly, A2 has the highest energy value among the four different structures. In general, the trend is $\Delta E_{L21} < \Delta E_{B2} < \Delta E_{A2}$ at 0 K. This indicates that the higher the degree of order is, the lower the energy and the more stable the structure at low temperatures. For the B2 $Ni_{50-x}Co_xFe_{25}Ga_{25}$ alloys with different Co contents, as shown in Fig. 3b1-b6, the FM state is more stable than the AFM state throughout the entire Bain path

considered in this work. This difference is entirely due to magnetic effects and not the structure or composition. However, the magnetic stability of the B2 structure is reversed in Fig. 3a1 for the $Ni_{50}Mn_{25}Ga_{25}$ alloy, which is more stable in the AFM state. Then, as the Co content increases, the FM and AFM states of the B2 structure compete with each other around $\varepsilon = 0\%$ (shown in Fig. 3a2). For the B2 structure ($\varepsilon = 0\%$), the FM state becomes more stable than the AFM state after the Co content reaches 10 at.%. For the B2 $Ni_{50-x}Co_xMn_{25}Ga_{25}$ alloys, the stable structure of the FM (AFM) state is austenite (unmodulated martensite). As shown in Fig. 3a3, when the Co content reaches 10 at.%, the stable B2 (FM) austenite competes with the stable B2 (AFM) unmodulated martensite. A similar situation occurs for the $L2_1$ (FM) $Ni_{50-x}Co_xMn_{25}Ga_{25}$ alloys. When the Co content is below 10 at.%, as shown in Fig. 3a1 and a2, the unmodulated martensite is more stable than the austenite. When the Co content is above 10 at.%, only austenite has an energy minimum. These results mean that both the $L2_1$ and B2 $Ni_{50-x}Co_xMn_{25}Ga_{25}$ alloys cannot undergo the martensite transformation when the Co content exceeds 10 at.%. This is consistent with the differential scanning calorimetry (DSC) and in situ synchrotron XRD experimental results by Cong et al. [66]. A few years ago, Wang et al. displayed a phase diagram of $Ni_{55-x}Co_xMn_{20}Ga_{25}$ alloys, which was determined by using DSC and dynamic mechanical analysis (DMA) [67]. In this phase diagram, the martensitic
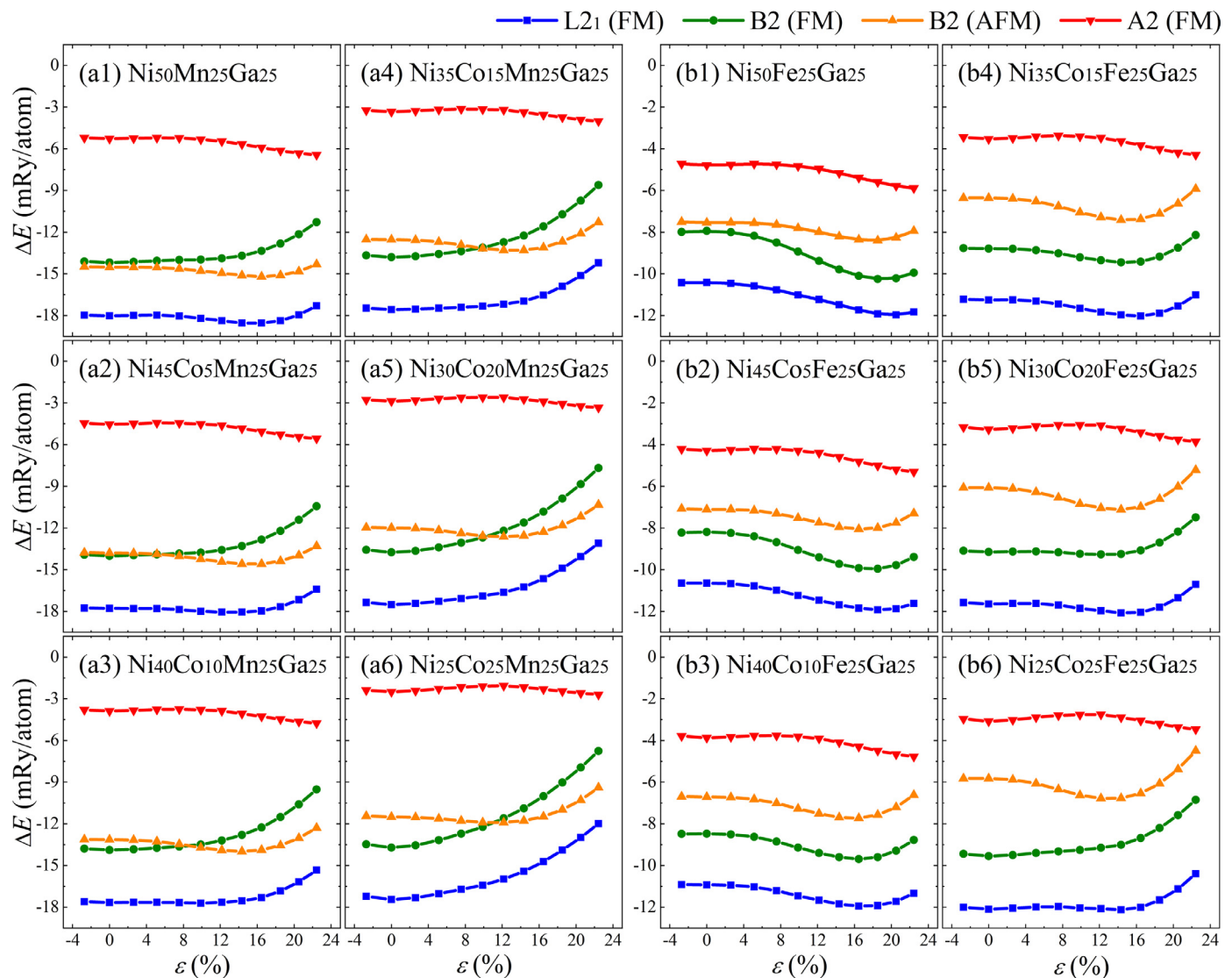
Fig. 3. The relative energy (ΔE) of $Ni_{50-x}Co_xMn_{25}Ga_{25}$ (the left two columns) and $Ni_{50-x}Co_xFe_{25}Ga_{25}$ (the right two columns) alloys as a function of strain (ε) for the tetragonal distortion of the $L2_1$, B2, and A2 cubic structures.

transition temperature (T_M) suddenly disappears at a critical Co content ($x_c \sim 10$ at.%). As shown in Fig. 3a3-a6, the total energies of FM and AFM $Ni_{50-x}Co_xMn_{25}Ga_{25}$ alloys ($10 \leq x \leq 25$ at.%) that adopt B2 structures have an intersection near $\varepsilon = 10\%$. According to the calculations for the B2 $Ni_{50-x}Co_xMn_{25}Ga_{25}$ alloys ($10 \leq x \leq 25$ at.%), we speculate that the FM austenite single crystal, as it is stretched along the <100> crystal direction, produces a magnetic transition from FM to AFM near $\varepsilon = 10\%$. The location of the magnetic transition shifts to larger strains with increasing Co content.

The relative phase stability of cubic austenite and corresponding unmodulated tetragonal martensite can be quantified by the energy difference between their two competing phases by considering $\Delta E_{A-M} = E_A - E_M$, where E_A and E_M are the *ab initio* total energies of the austenite and martensite phases, respectively. A positive value of ΔE_{A-M} indicates that the martensite phase is thermodynamically more stable than the austenite phase. According to the relationship $\Delta E_{A-M} \sim k_B T_M$, where k_B is the Boltzmann constant, ΔE_{A-M} and the martensitic transition temperature T_M have a positive linear correlation [68,69]. Our theoretical calculation values T_M are consistent with the available experimental values measured by Kanomata *et al.* [65] and Soto-Parra *et al.* [70]. It can

be seen in Fig. 4a that both the theoretically computed ΔE_{A-M} and the experimental T_M of $L2_1$ (FM) $Ni_{50-x}Co_xMn_{25}Ga_{25}$ alloys decrease almost linearly with increasing Co content. The measured T_M as a function of ΔE_{A-M} was fitted to the relation $T_M/K \approx -50 + 500\Delta E_{A-M}/(mRy/atom)$. This means that the addition of Co content reduces the stability of the martensite phase with respect to the austenite phase.

The number of valence electrons per atom (e/a) is a simple but effective indicator to describe the relationship between the element content and T_M. As shown in Fig. 4a, for $L2_1$ (FM) $Ni_{50-x}Co_xMn_{25}Ga_{25}$ alloys, a small e/a corresponds to a low T_M, which is consistent with previous studies [37,66,67]. The tetragonal shear modulus c' of the austenite phase is also considered to be an indicator to estimate the T_M. The martensite transformation is a consequence of the other phase having lower free energy at given temperature, is also thought to the result of phonon softening and corresponding softening of the shear modulus of the austenite phase. For unmodulated tetragonal martensite transformations, the soft shear modulus is the tetragonal shear modulus c'. A larger c' suggests a higher free energy of the martensite. Further suggests to inhibit the martensite transformation and thus re-
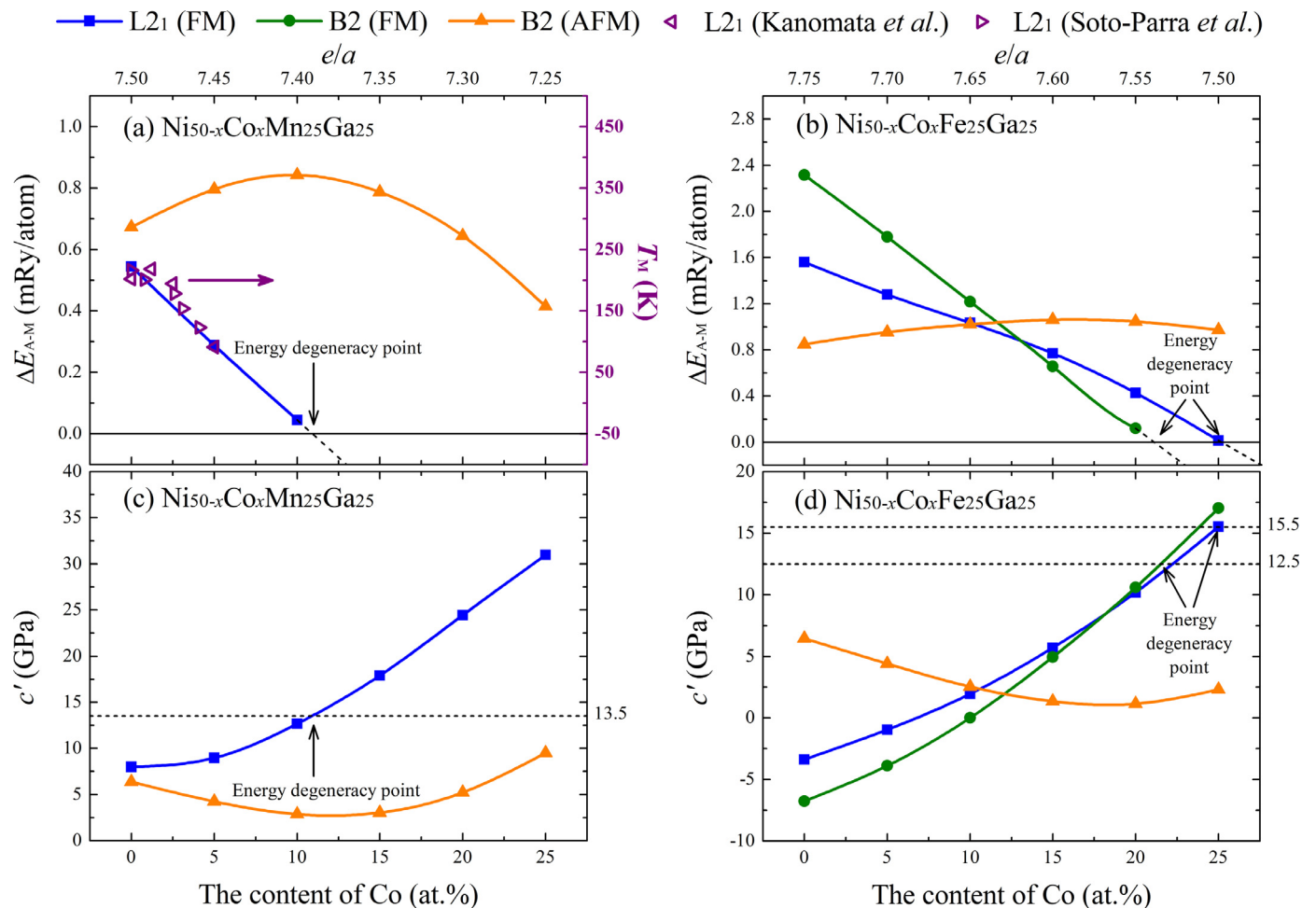
Fig. 4. The energy difference $\Delta E_{\text{A-M}}$ and the available experimental T_M with the purple ordinate (top) along with the tetragonal shear modulus c' (bottom) of $Ni_{50-x}Co_xMn_{25}Ga_{25}$ (left) and $Ni_{50-x}Co_xFe_{25}Ga_{25}$ (right) alloys as a function of Co content and e/a.

duces the T_M or even suppresses the martensite transformation completely [37]. This conclusion has also been rigorously proven by Ren *et al.* [71] using a Landau-type model. As shown in Fig. 4c, for $L2_1$ (FM) $Ni_{50-x}Co_xMn_{25}Ga_{25}$ alloys, c' increases monotonically with increasing Co content. Therefore, the T_M decreases monotonically with increasing Co content, which is in good agreement with the experimental results shown in Fig. 4a.

Since c' is negatively correlated with $\Delta E_{\text{A-M}}$, and $\Delta E_{\text{A-M}}$ is positively correlated with T_M, we can conclude that c' and T_M are negatively correlated. As shown in Fig. 4, for both B2 (AFM) $Ni_{50-x}Co_xMn_{25}Ga_{25}$ and $Ni_{50-x}Co_xFe_{25}Ga_{25}$ alloys, $\Delta E_{\text{A-M}}$ increases first and then decreases with increasing Co content. However, c' decreases first and then increases with increasing Co content. For the $L2_1$ (FM) $Ni_{50-x}Co_xMn_{25}Ga_{25}$, $L2_1$ (FM) $Ni_{50-x}Co_xFe_{25}Ga_{25}$, and B2 (FM) $Ni_{50-x}Co_xFe_{25}Ga_{25}$ alloys, all $\Delta E_{\text{A-M}}$ values decrease, whereas c' increases monotonically with increasing Co content. For these three alloys, the relationship between the $\Delta E_{\text{A-M}}$ and Co content is almost linear. By extending these lines with dashed lines, we can predict the Co content of the energy degeneracy of austenite and martensite at which the value of $\Delta E_{\text{A-M}}$ is zero. As shown in Fig. 4a, the Co content of the energy degeneracy of the $L2_1$ (FM) $Ni_{50-x}Co_xMn_{25}Ga_{25}$ alloy is approximately 11 at.%, and the corresponding c' is approximately 13.5 GPa. As shown in Fig. 4b and d, the Co contents of the energy degeneracy of the $L2_1$ (FM) and B2 (FM) $Ni_{50-x}Co_xFe_{25}Ga_{25}$ alloys are approximately 25 at.% and 21 at.%, and the corresponding c' values are approximately 15.5 GPa

and 12.5 GPa, respectively. Theoretically, superelasticity occurs in a certain alloy composition range after the energy degeneracy point. Therefore, only the alloys of the above three systems are likely to demonstrate superelasticity.

3.3. Nonhysteretic superelasticity

According to the Landau phase transformation theory, the free energy (F) of the martensitic transformation can be described by the Landau-de Gennes model:

$$F(P,\ T,\ \eta)\ =\ F_0\ +\ a(T\ -\ T_c)\eta^2\ +\ B\eta^3\ +\ C\eta^4, \quad (2)$$

where P is the pressure; T is the temperature; η is the order parameter; F_0 is the free energy with $\eta = 0$; and a (>0), B (<0), and C (>0) are coefficients for the 2-3-4-type Landau expansion of $F(P,\ T,\ \eta)$. T_c stands for the critical temperature at which the second-order phase transition occurs when the coefficient $B = 0$. In addition to the η^2 and η^4 terms of Landau theory, the free energy $F(P,\ T,\ \eta)$ includes a nonzero η^3 term, which ensures that it can be used to describe possible first-order phase transitions. Compared with the Landau-Devonshire model, which can also describe first-order phase transitions by the 2-4-6-type Landau expansion of $F(P,\ T,\ \eta)$, the Landau-de Gennes model can be applied to the case where order parameters η and $-\eta$ are not symmetric.
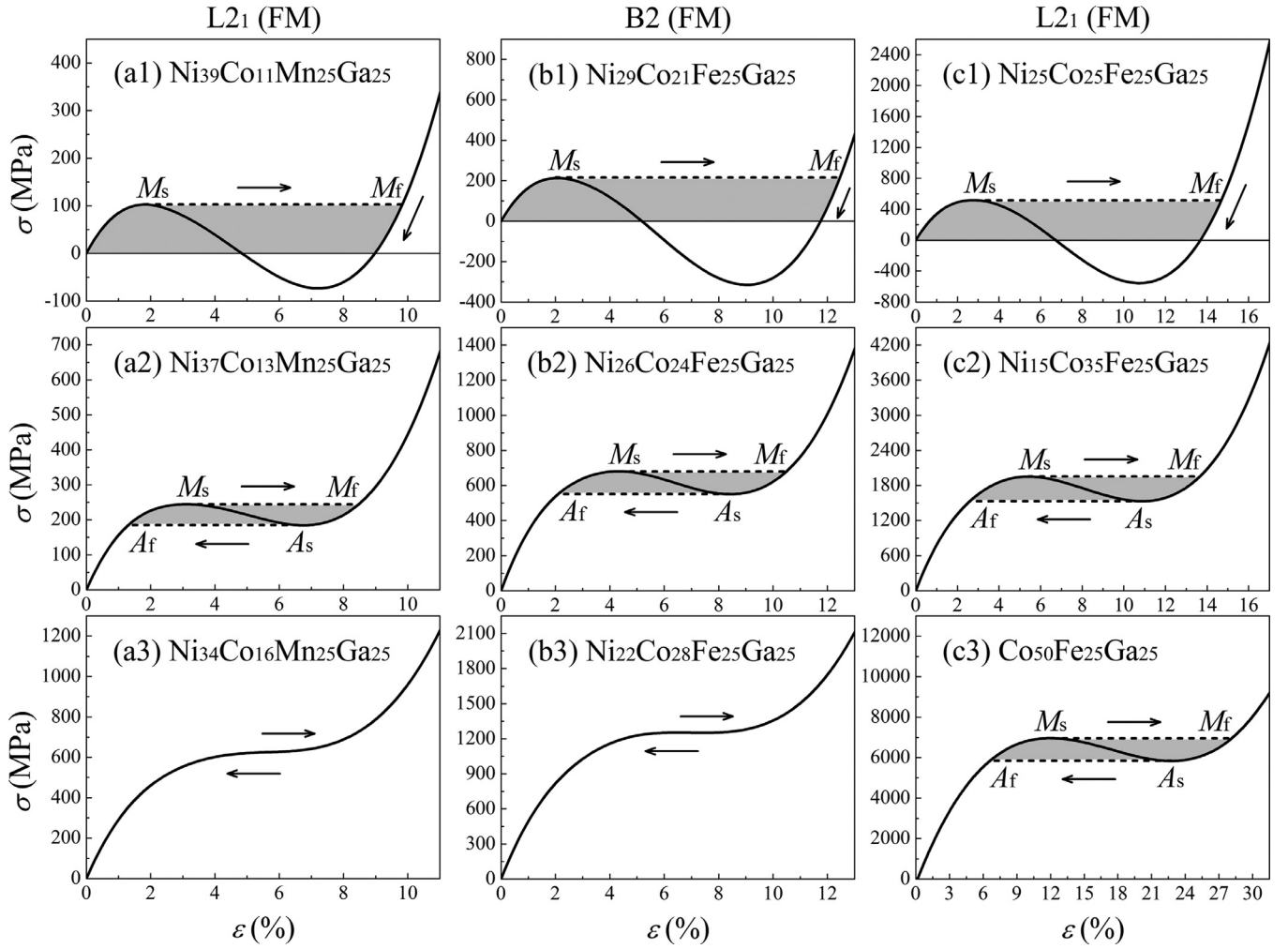
Fig. 5. The stress-strain curves obtained by theoretical calculation. The left column shows the stress-strain curves of the L2$_1$ (FM) Ni$_{50-x}$Co$_x$Mn$_{25}$Ga$_{25}$ alloys, the middle column shows the stress-strain curves of the B2 (FM) Ni$_{50-x}$Co$_x$Fe$_{25}$Ga$_{25}$ alloys, and the right column shows the stress-strain curves of the L2$_1$ (FM) Ni$_{50-x}$Co$_x$Fe$_{25}$Ga$_{25}$ alloys.

Upon omitting both the pressure and temperature in the present *ab initio* based investigation, we can simplify Eq. (2) as

$$E(\varepsilon) = E_0 + A\varepsilon^2 + B\varepsilon^3 + C\varepsilon^4, \tag{3}$$

where $E(\varepsilon)$ is the *ab initio* total energy, E_0 is the total energy of the structure with $\varepsilon = 0$, $A = -aT_c$, and B (<0) and C (>0) are the composition-dependent coefficients. Note that the order parameter η is the strain (ε) for the tetragonal distortion along the Bain path. The stress (σ) value can be obtained by taking the first derivative of Eq. (3):

$$\sigma = \frac{1}{V}\frac{dE(\varepsilon)}{d\varepsilon}. \tag{4}$$

Fig. 5 shows a series of stress-strain curves obtained by the theoretical calculation of different Co contents. The stress-strain curve of L2$_1$ (FM) Ni$_{39}$Co$_{11}$Mn$_{25}$Ga$_{25}$ alloy which has the Co content for energy degeneracy mentioned above is shown in Fig. 5a1. At the initial stage of the loading stress, the austenite phase undergoes elastic deformation until the stress reaches 103 MPa and the strain reaches 1.8%. After that, the martensite transformation occurs gradually in the austenite phase. Until the strain reaches 9.8%, the austenite phase completely transforms to the martensite phase. After the region of the horizontal dashed line (from the start of the martensite transformation M_s to the end of martensite transformation M_f), the martensite phase continues to undergo elastic deformation until the material breaks. If the stress is unloaded before the material breaks, the martensite phase remains intact and produces a permanent strain of 9.0%. This shows an irreversible inelastic deformation with applied stress unless a temperature rise causes the material to undergo an inverse martensitic transformation. If the content of Co is appropriately added based on the Co content-dependent energy degeneracy, we can obtain the stress-strain curve shown in Fig. 5a2. With an increase in the applied stress, the stress-strain curve also goes through the above three stages: (1) the austenite phase undergoes elastic deforma-
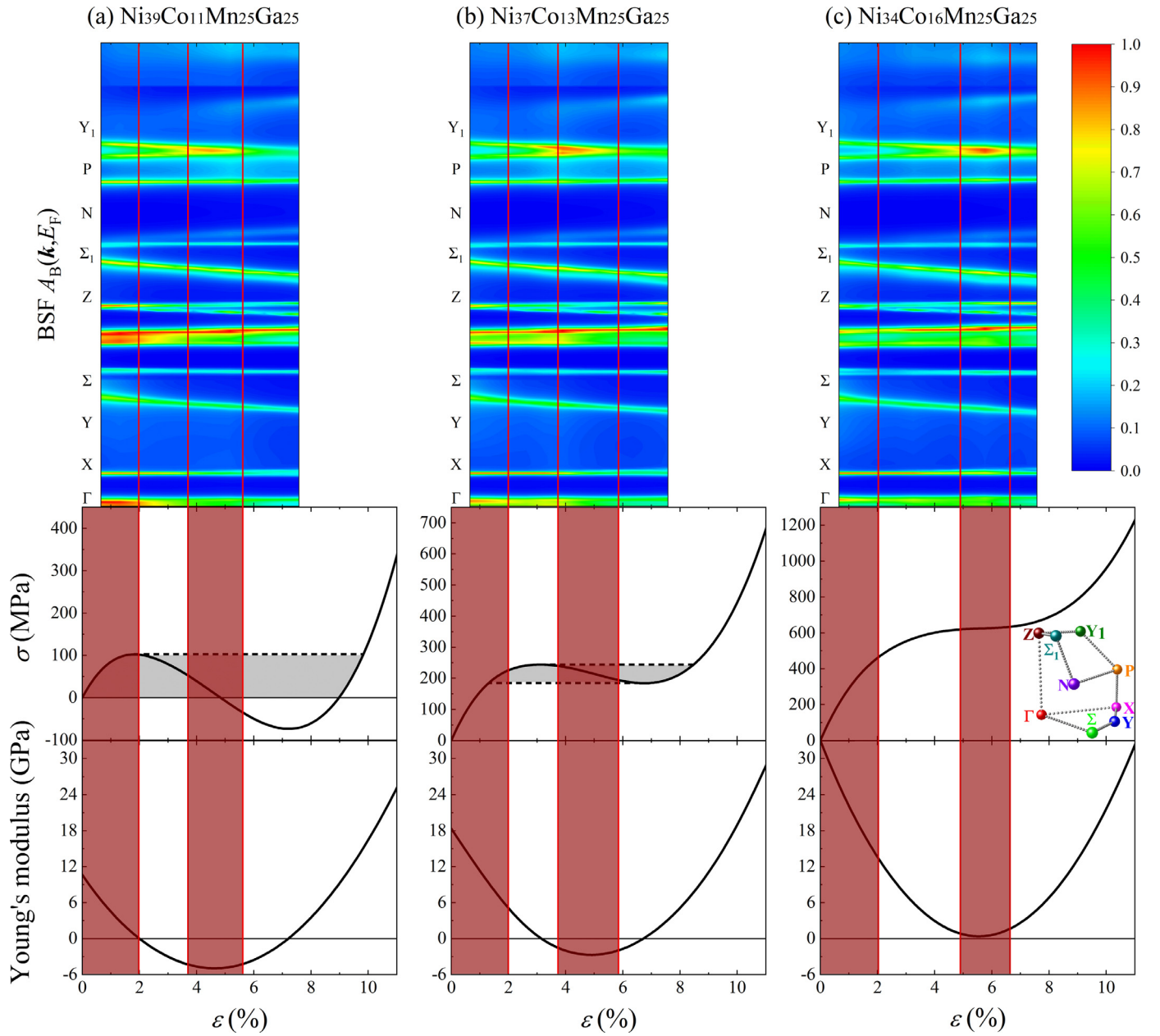
Table 2
The tensile strength σ at a strain of 10% and Young's modulus E along the $<100>$ crystal direction for the present alloys and bcc metals and alloys. Co$_{16}$ represents L2$_1$ (FM) Ni$_{34}$Co$_{16}$Mn$_{25}$Ga$_{25}$, and Co$_{28}$ represents B2 (FM) Ni$_{22}$Co$_{28}$Fe$_{25}$Ga$_{25}$. σ_m stands for the ideal tensile strength.

	σ_m (GPa)	σ (GPa)	E_{100} (GPa)	σ/E_{100}	Ref.
Co$_{16}$	–	0.9	55.3	0.016	–
Co$_{28}$	–	1.3	61.1	0.021	–
V	16.7	13.7	147.2	0.093	[76]
Nb	13.1	12.5	151.5	0.082	[77,78]
Mo	28.8	27.1	383.6	0.071	[77,78]
W	28.9	27.7	407.4	0.068	[79]
Fe	12.6	10.7	118.9	0.090	[80,81]
Ti$_3$V	1.8	1.6	18.6	0.086	[76]
Ti$_{11}$V$_9$	5.1	4.5	53.1	0.085	[76]
Ti$_3$V$_7$	10.2	8.5	104.0	0.082	[76]
Ti$_3$Nb	2.5	2.3	53.4	0.043	[82]

Fig. 6. The evaluated Bloch spectral function along the reciprocal space path **Γ-X-Y-Σ-Z-Σ₁-N-P-Y₁** at the Fermi energy (top) for different tensile strains ε. Red vertical lines mark substantial changes in the Fermi surface, which may be correlated to variations of the stress (middle) and Young's modulus (bottom). Different connected regimes are emphasised by changing shades of dark red and white. Subfigure a-c correspond to Fig. 5a1-a3, respectively.

tion until the stress reaches 245 MPa and the strain reaches 3.1%; (2) the austenite is gradually transformed into martensite from M_s ($\varepsilon = 3.1\%$) to M_f ($\varepsilon = 8.5\%$); and (3) the martensite phase continues to undergo elastic deformation until the material breaks. However, before the material breaks, the deformation behavior after unloading the stress is different from that shown in Fig. 5a1. The martensite phase is gradually transformed into austenite from A_s ($\varepsilon = 6.7\%$) to A_f ($\varepsilon = 1.3\%$) under the stress of 186 MPa. Finally, the $Ni_{37}Co_{13}Mn_{25}Ga_{25}$ alloy returns to its original shape and exhibits superelasticity with hysteresis (gray area). The stress-strain curves of the B2 and L2₁ (FM) $Ni_{50-x}Co_xFe_{25}Ga_{25}$ alloys, which have the Co content of energy degeneracy mentioned above, are shown in Fig. 5b1 and c1, respectively. These show an irreversible inelastic deformation with applied stress. After an appropriate increase in Co content, as shown in Fig. 5b2 and c2, the stress-strain curves exhibit superelasticity with hysteresis (gray area).

The stress-induced first-order martensite phase transformations are shown in both Fig. 5a1 and a2 which have a sudden lattice deformation under an applied stress. As the Co content increases, this phenomenon disappears. As shown in Fig. 5a3, when the Co content reaches 16 at.%, the gray area disappears, and nonhysteretic superelasticity occurs. In this case, a continuous lattice change replaces the structural mutation induced by the first-order phase transition during the stress loading and unloading. As shown in Fig. 5b3, a similar process also occurs in the B2 (FM) $Ni_{22}Co_{28}Fe_{25}Ga_{25}$ alloy. However, for L2₁ (FM) $Ni_{22}Co_{28}Fe_{25}Ga_{25}$ alloy, as shown in Fig. 5c3, even if all Ni atoms are replaced by Co atoms, the first-order phase transition cannot be avoided. Both the L2₁ (FM) $Ni_{34}Co_{16}Mn_{25}Ga_{25}$ and B2 (FM) $Ni_{22}Co_{28}Fe_{25}Ga_{25}$ alloys have very small stress values in the case of a large strain due to the existence of nonhysteretic superelasticity. These two alloys have only 0.9 GPa and 1.3 GPa stresses when the strain reaches
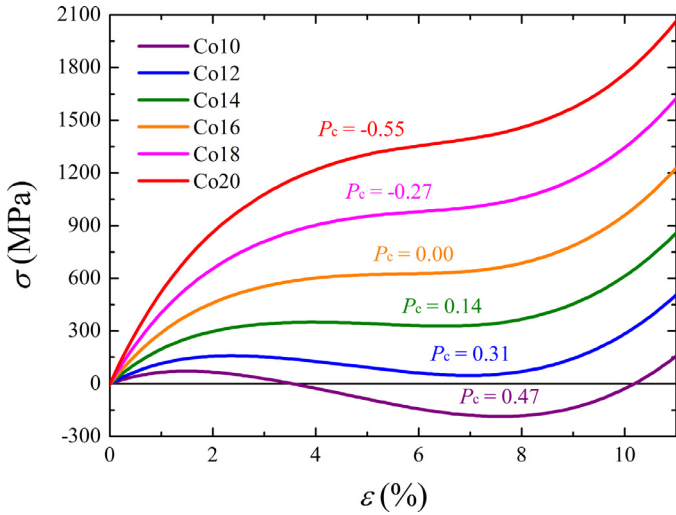
Fig. 7. The stress-strain curves of the L2$_1$ (FM) Ni$_{50-x}$Co$_x$Mn$_{25}$Ga$_{25}$ alloys with different Co contents accompanied by their respective P_c values.

10%, which ensures that the material is not prone to fracture in the case of a large deformation. To our knowledge, such small stresses have not been found in previous theoretical calculations of bcc metals and alloys. Table 2 lists the available *ab initio* calculations for the tensile strength σ and Young's modulus E along the <100> crystal direction. σ at a strain of 10% is close to the ideal tensile strength σ_m. The σ/E_{100} ratio is approximately 0.07~0.09 for bcc metals and alloys, except for Ti$_3$Nb, which is consistent with the theoretical value of $\sigma_m/E_{100} = e_B/\pi \approx 0.08$ [72-74]. According to the theories by Frenkel [1] and Orowan [75], the stress-strain curve was approximated to a sinusoidal form with the period of e_B. For bcc to fcc stretching along the Bain path, the value of e_B is approximately 0.26. However, for the present alloys, the σ/E_{100} ratio is small. This indicates that the tensile strength at a strain of 10% may be much smaller than the ideal tensile strength. The present work demonstrates for the first time using *ab initio* calculations that the stress level can remain below 1 GPa when the strain reaches 10% without the occurrence of a phase transition.

In order to further understand the evolution of nonhysteretic superelasticity, we investigate the detailed electronic structure of the system and focus on the changes in the Fermi surface topology obtained from Bloch spectral function (BSF) calculations. We show the BSF evaluated at the Fermi energy E_F for each tensile strain and Young's modulus of the corresponding stress-strain curve in Fig. 6. The vertical red lines indicate the microscopic changes in

the Fermi surface, which is associated with the key changes of macroscopic stress-strain curve and Young's modulus. We can find that two bands between P and Y$_1$ points become left degenerate (see the second vertical red line). It may suggest there exists the electronic topology transition (ETT) around some tensile strain. For example, the ETT occur at $\varepsilon = 6\%$ for Ni$_{34}$Co$_{16}$Mn$_{25}$Ga$_{25}$ with non-hysteretic superelasticity. Comparing three different concentrations Ni$_{39}$Co$_{11}$Mn$_{25}$Ga$_{25}$, Ni$_{37}$Co$_{13}$Mn$_{25}$Ga$_{25}$, and Ni$_{34}$Co$_{16}$Mn$_{25}$Ga$_{25}$ alloys, the degenerated band is corresponding to different tensile strains. The changes of strong BSF around the path Σ-Z (see the first vertical red line) occur for the tensile strain $\varepsilon < 2\%$. At the same time the resolved peaks around the path P-Y$_1$ are shown between the second and third red lines, where the minimum of Young's modulus happens to exist for the three concentrations.

3.4. Critical parameter

As shown in Fig. 6, a negative Young's modulus ($\frac{d^2E(\varepsilon)}{d\varepsilon^2} < 0$) leads to mechanical instability, resulting in irreversible inelastic deformation or superelasticity with hysteresis under the action of applied stress. The inflection point of mechanical instability occurs at the strain position where Young's modulus is zero ($\frac{d^2E(\varepsilon)}{d\varepsilon^2} = 0$). Only by ensuring that Young's modulus is always non-negative ($\frac{d^2E(\varepsilon)}{d\varepsilon^2} > 0$), so that the material always maintains mechanical stability, can the nonhysteretic superelasticity be obtained. The Young's modulus and stress-strain curves of the Ni$_{50-x}$Co$_x$Mn$_{25}$Ga$_{25}$ and Ni$_{50-x}$Co$_x$Fe$_{25}$Ga$_{25}$ alloys are strongly dependent on the change of Co content (x). In terms of material design, we expect to obtain an ideal nonhysteretic superelastic material by studying as few components as possible. To this end, we introduce the critical parameter (P_c):

$$P_c = 3B^2 - 8AC, \tag{5}$$

where A, B, and C are the composition-dependent coefficients of Eq. (3). The parameter $P_c = 0$ is the critical point where the Young's modulus along the <100> direction is always nonnegative, which is the necessary condition for nonhysteresis. As shown in Fig. 7, in the range of $P_c \leq 0$ ($x \geq 16$ at.%), a nonhysteretic superelasticity occurs for the corresponding composition. However, in the range of $P_c > 0$ ($x < 16$ at.%), a stress-induced first-order martensite phase transformation occurs for this composition, and the structure mutates under an applied stress. As shown in Fig. 8, the values of P_c are linearly correlated with the Co content. Using linear curve fitting and extending the existing values, we can predict the corresponding composition of the critical point when $P_c = 0$. For the L2$_1$ (FM) Ni$_{50-x}$Co$_x$Mn$_{25}$Ga$_{25}$ alloys, as shown in Fig. 8a, the Co content of the critical point is 16 at.%, which is consistent with
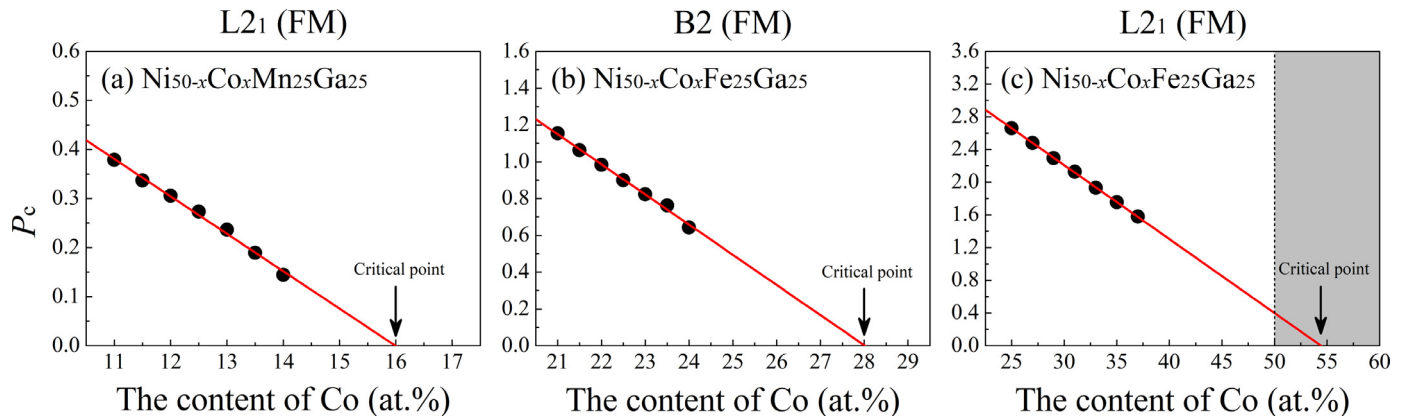

Fig. 8. The values of P_c for the Ni based Heusler alloys as a function of Co content.

the results in Fig. 7. Its corresponding stress-strain curve is shown in Fig. 5a3. Similarly, for the B2 (FM) $Ni_{50-x}Co_xFe_{25}Ga_{25}$ alloys, as shown in Fig. 8b, the Co content of the critical point is 28 at.%. Its corresponding stress-strain curve is shown in Fig. 5b3. However, for the L2$_1$ (FM) $Ni_{50-x}Co_xFe_{25}Ga_{25}$ alloys, the Co content of the critical point is 54 at.%, which exceeds the maximum allowable value of 50 at.% of the alloy composition. Therefore, it is impossible for the stress-strain curve to exhibit nonhysteretic superelasticity for L2$_1$ (FM) $Ni_{50-x}Co_xFe_{25}Ga_{25}$ alloys, even for the $Co_{50}Fe_{25}Ga_{25}$ alloy shown in Fig. 5c3.

4. Conclusions

In this paper, we investigate the effects of element content and disorder degree on nonhysteretic superelasticity behaviors of $Ni_{50-x}Co_xM_{25}Ga_{25}$ (M = Mn, Fe) Heusler alloys by employing the *ab initio* EMTO method in connection with alloy theory formulated using the CPA. The equilibrium properties of the L2$_1$ austenite and the corresponding martensite in Ni_2MnGa and Ni_2FeGa are analyzed systematically. The reliability of the EMTO-CPA method in the calculation of such alloys is verified by a comparison with other experimental and calculated results. By analyzing the energy-strain curve, it is found that magnetic reversal (FM ↔ AFM) may occur with the stretching of $Ni_{50-x}Co_xMn_{25}Ga_{25}$ alloys with B2 structures. For the $Ni_{50-x}Co_xMn_{25}Ga_{25}$ alloys with L2$_1$ and B2 structures, a Co content of approximately 10 at.% is the inflection point for inhibiting the martensite transformation, which is consistent with the previous experimental results. We analyze the relationship between ΔE_{A-M}, e/a, c', and T_M which can be used to directly predict the critical Co content of the martensitic phase transformation disappearance (energy degeneracy point). The most important finding is that the structure and composition range of superelastic materials without hysteresis can be predicted by calculating the critical parameter P_c. For the ferromagnetic L2$_1$ $Ni_{50-x}Co_xMn_{25}Ga_{25}$ and B2 $Ni_{50-x}Co_xFe_{25}Ga_{25}$ alloys, we predict that the nonhysteretic superelasticity occurs after the Co content exceeds 16 at.% and 28 at.%, respectively.

Declaration of Competing Interest

The authors declare that they have no known competing financial interests or personal relationships that could have appeared to influence the work reported in this paper.

Acknowledgments

References

[1] J. Frenkel, Zur Theorie der Elastizitätsgrenze und der Festigkeit kristallinischer Körper, Z. Phys. 37 (7) (1926) 572–609.

[2] H. Zhang, J. Tersoff, S. Xu, H. Chen, Q. Zhang, K. Zhang, Y. Yang, C.-S. Lee, K.-N. Tu, J. Li, Y. Lu, Approaching the ideal elastic strain limit in silicon nanowires, Science Advances 2 (8) (2016) e1501382.

[3] Y. Tanaka, Y. Himuro, R. Kainuma, Y. Sutou, T. Omori, K. Ishida, , Ferrous Poly-crystalline Shape-Memory Alloy Showing Huge Superelasticity, Science 327 (5972) (2010) 1488–1490.

[4] T.W. Duerig, A.R. Pelton, D. Stockel, The utility of superelasticity in medicine, Bio-Med. Mater. Eng. 6 (4) (1996) 255–266.

[5] R.B. Pérez-Sáez, V. Recarte, M.L. Nó, J. San Juan, Anelastic contributions and transformed volume fraction during thermoelastic martensitic transformations, Phys Rev B 57 (10) (1998) 5684–5692.

[6] J. Van Humbeeck, Damping capacity of thermoelastic martensite in shape memory alloys, J. Alloys Compd. 355 (1-2) (2003) 58–64.

[7] A. Kosogor, V.A. L'vov, V.A. Chernenko, E. Villa, J.M. Barandiaran, T. Fukuda, T. Terai, T. Kakeshita, Hysteretic and anhysteretic tensile stress-strain behavior of Ni-Fe(Co)-Ga single crystal: Experiment and theory, Acta Mater 66 (2014) 79–85.

[8] T. Waitz, V. Kazykhanov, H.P. Karnthaler, Martensitic phase transformations in nanocrystalline NiTi studied by TEM, Acta Mater 52 (1) (2004) 137–147.

[9] T. Waitz, T. Antretter, F.D. Fischer, N.K. Simha, H.P. Karnthaler, Size effects on the martensitic phase transformation of NiTi nanograins, J. Mech. Phys. Solids 55 (2) (2007) 419–444.

[10] Z. Zhang, X.D. Ding, J. Sun, T. Suzuki, T. Lookman, K. Otsuka, X.B. Ren, Non-hysteretic Superelasticity of Shape Memory Alloys at the Nanoscale, Phys. Rev. Lett. 111 (14) (2013) 145701.

[11] L.F. Liu, X.D. Ding, J. Li, T. Lookman, J. Sun, Direct observation of hierarchical nucleation of martensite and size-dependent superelasticity in shape memory alloys, Nanoscale 6 (4) (2014) 2067–2072.

[12] L.F. Liu, X.D. Ding, J. Sun, S.Z. Li, E.K.H. Salje, Breakdown of Shape Memory Effect in Bent Cu-Al-Ni Nanopillars: When Twin Boundaries Become Stacking Faults, Nano Lett 16 (1) (2016) 194–198.

[13] K. Asaka, Y. Hirotsu, T. Tadaki, Structure of nanometer-sized Au-Cd alloy particles near equiatomic compositions at room temperature, Mat Sci Eng a-Struct 312 (1-2) (2001) 232–236.

[14] K. Seki, H. Kura, T. Sato, T. Taniyama, Size dependence of martensite transformation temperature in ferromagnetic shape memory alloy FePd, J. Appl. Phys. 103 (6) (2008) 063910.

[15] H. Chen, Y.D. Wang, Z. Nie, R. Li, D. Cong, W. Liu, F. Ye, Y. Liu, P. Cao, F. Tian, X. Shen, R. Yu, L. Vitos, M. Zhang, S. Li, X. Zhang, H. Zheng, J.F. Mitchell, Y. Ren, Unprecedented non-hysteretic superelasticity of [001]-oriented NiCoFeGa single crystals, Nat Mater 19 (7) (2020) 712–718.

[16] W.H. Wang, G.H. Wu, J.L. Chen, C.H. Yu, S.X. Gao, W.S. Zhan, Z. Wang, Z.Y. Gao, Y.F. Zheng, L.C. Zhao, Stress-free two-way thermoelastic shape memory and field-enhanced strain in Ni52Mn24Ga24 single crystals, Appl. Phys. Lett. 77 (20) (2000) 3245–3247.

[17] W.H. Wang, Z.H. Liu, Z.W. Shan, J.L. Chen, G.H. Wu, W.S. Zhan, Effect of post–growth annealing and magnetic field on the two-way shape memory effect of Ni52Mn24Ga24 single crystals, J Phys D Appl Phys 35 (5) (2002) 492–496.

[18] V.A. Chernenko, V. L'vov, J. Pons, E. Cesari, Superelasticity in high-temperature Ni-Mn-Ga alloys, J. Appl. Phys. 93 (5) (2003) 2394–2399.

[19] K. Ullakko, J.K. Huang, C. Kantner, R.C. O'Handley, V.V. Kokorin, Large magnet-ic-field-induced strains in Ni2MnGa single crystals, Appl. Phys. Lett. 69 (13) (1996) 1966–1968.

[20] S.J. Murray, M.A. Marioni, A.M. Kukla, J. Robinson, R.C. O'Handley, S.M. Allen, Large field induced strain in single crystalline Ni-Mn-Ga ferromagnetic shape memory alloy, J. Appl. Phys. 87 (9) (2000) 5774–5776.

[21] K. Oikawa, T. Ota, Y. Sutou, T. Ohmori, R. Kainuma, K. Ishida, Magnetic and martensitic phase transformations in a Ni54Ga27Fe19 alloy, Mater Trans 43 (9) (2002) 2360–2362.

[22] H. Morito, A. Fujita, K. Oikawa, K. Ishida, K. Fukamichi, R. Kainuma, Stress-as-sisted magnetic-field-induced strain in Ni-Fe-Ga-Co ferromagnetic shape memory alloys, Appl. Phys. Lett. 90 (6) (2007) 062505.

[23] B.M. Wang, P. Ren, Y. Liu, L. Wang, Enhanced magnetoresistance through magnetic-field-induced phase transition in Ni2MnGa co-doped with Co and Mn, J. Magn. Magn. Mater. 322 (6) (2010) 715–717.

[24] D.P. Wang, X. Chen, Z.H. Nie, N. Li, Z.L. Wang, Y. Ren, Y.D. Wang, Transition in superelasticity for Ni55-xCoxFe18Ga27 alloys due to strain glass transition, Epl-Europhys Lett 98 (4) (2012) 46004.

[25] Z.Y. Ding, D.X. Liu, Q.L. Qi, J.X. Zhang, Y.L. Yao, Y. Zhang, D.Y. Cong, J. Zhu, Multistep superelasticity of Ni-Mn-Ga and Ni-Mn-Ga-Co-Cu microwires under stress-temperature coupling, Acta Mater 140 (2017) 326–336.

[26] L. Vitos, Computational Quantum Mechanics for Materials Engineers-The EMTO Method and Applications, Springer London, 2007.

[27] L. Vitos, Total-energy method based on the exact muffin-tin orbitals theory, Phys Rev B 64 (1) (2001) 014107.

[28] L. Vitos, H.L. Skriver, B. Johansson, J. Kollár, Application of the exact muffin-tin orbitals theory: the spherical cell approximation, Comp Mater Sci 18 (1) (2000) 24–38.

[29] L. Vitos, I.A. Abrikosov, B. Johansson, Anisotropic lattice distortions in random alloys from first-principles theory, Phys. Rev. Lett. 87 (15) (2001) 156401.

[30] B.L. Gyorffy, Coherent-Potential Approximation for a Nonoverlapping-Muffin-T-in-Potential Model of Random Substitutional Alloys, Phys Rev B 5 (6) (1972) 2382–2384.

[31] P. Soven, Coherent-Potential Model of Substitutional Disordered Alloys, Phys. Rev. 156 (3) (1967) 809–813.

[32] D.D. Johnson, D.M. Nicholson, F.J. Pinski, B.L. Gyorffy, G.M. Stocks, Density–Functional Theory for Random Alloys: Total Energy within the Coherent-Potential Approximation, Phys. Rev. Lett. 56 (19) (1986) 2088–2091.

[33] G.M. Stocks, W.M. Temmerman, B.L. Gyorffy, Complete Solution of the Korringa-Kohn-Rostoker Coherent-Potential-Approximation Equations: Cu-Ni Alloys, Phys. Rev. Lett. 41 (5) (1978) 339–343.

[34] M. Yin, P. Nash, W. Chen, S. Chen, Standard enthalpies of formation of selected Ni(2)YZ Heusler compounds, J. Alloys Compd. 660 (2016) 258–265.

[35] P. Neibecker, M.E. Gruner, X. Xu, R. Kainuma, W. Petry, R. Pentcheva, M. Leit-

ner, Ordering tendencies and electronic properties in quaternary Heusler derivatives, Phys Rev B 96 (16) (2017) 165131.

[36] T.M. Heil, M.A. Willard, W.T. Reynolds, The effects of composition and aging on the martensite and magnetic transformations in Ni-Fe-Ga ferromagnetic shape memory alloys, Metall Mater Trans A 38A (4) (2007) 752–758.

[37] H.B. Luo, C.M. Li, Q.M. Hu, R. Yang, B. Johansson, L. Vitos, Theoretical investigation of the effects of composition and atomic disordering on the properties of Ni2Mn(Al1-xGax) alloy, Acta Mater 59 (3) (2011) 971–980.

[38] J.P. Perdew, K. Burke, M. Ernzerhof, Generalized Gradient Approximation Made Simple, Phys. Rev. Lett. 77 (18) (1996) 3865–3868.

[39] S.Y. Savrasov, D.Y. Savrasov, Full-potential linear-muffin-tin-orbital method for calculating total energies and forces, Physical Review B (Condensed Matter) 46 (19) (1992) 12181–12195.

[40] S.Y. Savrasov, Linear-response theory and lattice dynamics: a muffin-tin-orbital approach, Physical Review B (Condensed Matter) 54 (23) (1996) 16470–16486.

[41] J.P. Perdew, Y. Wang, Pair-distribution function and its coupling-constant average for the spin-polarized electron gas, Physical Review B (Condensed Matter) 46 (20) (1992) 12947–12954.

[42] J.P. Perdew, A. Zunger, Self-interaction correction to density-functional approximations for many-electron systems, Physical Review B (Condensed Matter) 23 (10) (1981) 5048–5079.

[43] P.J. Webster, K.R.A. Ziebeck, S.L. Town, M.S. Peak, Magnetic order and phase transformation in Ni2MnGa, Philosophical Magazine B (Physics of Condensed Matter, Electronic, Optical and Magnetic Properties) 49 (3) (1984) 295–310.

[44] J. Worgull, E. Petti, J. Trivisonno, Behavior of the elastic properties near an intermediate phase transition in Ni2MnGa, Phys Rev B 54 (22) (1996) 15695–15699.

[45] P.J. Brown, J. Crangle, T. Kanomata, M. Matsmuoto, K.U. Neumann, B. Ouladdiaf, K.R.A. Ziebeck, The crystal structure and phase transitions of the magnetic shape memory compound Ni2MnGa, J Phys-Condens Mat 14 (43) (2002) 10159–10171.

[46] L. Mañosa, A. Gonz'alez-Comas, E. Obradó, A. Planes, V.A. Chernenko, V.V. Kokorin, E. Cesari, Anomalies related to the TA2-phonon-mode condensation in the Heusler Ni2MnGa alloy, Phys Rev B 55 (17) (1997) 11068–11071.

[47] H. Rached, D. Rached, R. Khenata, A.H. Reshak, M. Rabah, First-principles calculations of structural, elastic and electronic properties of Ni(2)MnZ (Z = Al, Ga and In) Heusler alloys, Phys Status Solidi B 246 (7) (2009) 1580–1586.

[48] C. Bungaro, K.M. Rabe, A.D. Corso, First-principles study of lattice instabilities in ferromagnetic Ni2MnGa, Phys Rev B 68 (13) (2003) 134104.

[49] A. Ayuela, J. Enkovaara, K. Ullakko, R.M. Nieminen, Structural properties of magnetic Heusler alloys, Journal of Physics: Condensed Matter 11 (8) (1999) 2017–2026.

[50] Q.M. Hu, H.B. Luo, C.M. Li, L. Vitos, R. Yang, Composition dependent elastic modulus and phase stability of Ni2MnGa based ferromagnetic shape memory alloys, Sci China Technol Sc 55 (2) (2012) 295–305.

[51] J. Bai, J.M. Raulot, Y.D. Zhang, C. Esling, X. Zhao, L. Zuo, Crystallographic, magnetic, and electronic structures of ferromagnetic shape memory alloys Ni2XGa (X=Mn, Fe, Co) from first-principles calculations, J. Appl. Phys. 109 (1) (2011) 014908.

[52] Y. Qawasmeh, B. Hamad, Investigation of the structural, electronic, and magnetic properties of Ni-based Heusler alloys from first principles, J. Appl. Phys. 111 (3) (2012) 033905.

[53] J. Bai, J.M. Raulot, Y.D. Zhang, C. Esling, X. Zhao, L. Zuo, The effects of alloying element Co on Ni-Mn-Ga ferromagnetic shape memory alloys from first-principles calculations, Appl. Phys. Lett. 98 (16) (2011) 164103.

[54] V.V. Martynov, V.V. Kokorin, The crystal structure of thermally- and stress-induced martensites in Ni2MnGa single crystals, Journal de Physique III (Applied Physics, Materials Science, Fluids, Plasma and Instrumentation) 2 (5) (1992) 739–749.

[55] A.T. Zayak, P. Entel, J. Enkovaara, A. Ayuela, R.M. Nieminen, First-principles investigations of homogeneous lattice-distortive strain and shuffles in Ni2MnGa, J Phys-Condens Mat 15 (2) (2003) 159–164.

[56] A. Ayuela, J. Enkovaara, R.M. Nieminen, Ab initio study of tetragonal variants in Ni2MnGa alloy, J Phys-Condens Mat 14 (21) (2002) 5325–5336.

[57] Z.H. Liu, M. Zhang, Y.T. Cui, Y.Q. Zhou, W.H. Wang, G.H. Wu, X.X. Zhang, G. Xiao, Martensitic transformation and shape memory effect in ferromagnetic Heusler alloy Ni2FeGa, Appl. Phys. Lett. 82 (3) (2003) 424–426.

[58] Z.H. Liu, H.N. Hu, G.D. Liu, Y.T. Cui, M. Zhang, J.L. Chen, G.H. Wu, G. Xiao, Electronic structure and ferromagnetism in the martensitic-transformation material Ni2FeGa, Phys Rev B 69 (13) (2004) 134415.

[59] Y. Sutou, N. Kamiya, T. Omori, R. Kainuma, K. Ishida, K. Oikawa, Stress-strain characteristics in Ni-Ga-Fe ferromagnetic shape memory alloys, Appl Phys Lett 84 (8) (2004) 1275–1277.

[60] Z.W. Du, B.L. Shao, A.S. Liu, G.H. Wu, J.F. Qian, Z.Y. Zhang, Z. Gao, Martensitic transition and structural modulations in Ni51Fe24Ga25 ferromagnetic shape-memory alloy, J Mater Sci 46 (8) (2011) 2733–2740.

[61] J.I. Perez-Landazabal, V. Recarte, V. Sanchez-Alarcos, J.A. Rodriguez-Velamazan, M. Jimenez-Ruiz, P. Link, E. Cesari, Y.I. Chumlyakov, Lattice dynamics and external magnetic-field effects in Ni-Fe-Ga alloys, Phys Rev B 80 (14) (2009) 144301.

[62] H. Sehitoglu, J. Wang, H.J. Maier, Transformation and slip behavior of Ni2FeGa, Int. J. Plast. 39 (2012) 61–74.

[63] C. Soykan, S.O. Kart, C. Sevik, T. Cagin, Ab initio calculations of martensitic phase behavior in Ni2FeGa magnetic shape memory alloys, J Alloy Compd 611 (2014) 225–234.

[64] M.B. Sahariah, S. Ghosh, C.S. Singh, S. Gowtham, R. Pandey, First-principles computation of structural, elastic and magnetic properties of Ni2FeGa across the martensitic transformation, J Phys-Condens Mat 25 (2) (2013) 025502.

[65] T. Kanomata, Y. Kitsunai, K. Sano, Y. Furutani, H. Nishihara, R.Y. Umetsu, R. Kainuma, Y. Miura, M. Shirai, Magnetic properties of quaternary Heusler alloys Ni2-xCoxMnGa, Phys Rev B 80 (21) (2009) 214402.

[66] D.Y. Cong, S. Wang, Y.D. Wang, Y. Ren, L. Zuo, C. Esling, Martensitic and magnetic transformation in Ni-Mn-Ga-Co ferromagnetic shape memory alloys, Mat Sci Eng a-Struct 473 (1-2) (2008) 213–218.

[67] Y. Wang, C.H. Huang, J.H. Gao, S. Yang, X.D. Ding, X.P. Song, X.B. Ren, Evidence for ferromagnetic strain glass in Ni-Co-Mn-Ga Heusler alloy system, Appl. Phys. Lett. 101 (10) (2012) 101913.

[68] V.V. Sokolovskiy, M.A. Zagrebin, V.D. Buchelnikov, P. Entel, The Effect of Anti-Site Disorder on Structural and Magnetic Properties of Ni-Co-Mn-In Alloys: Ab Initio and Monte Carlo Studies, IEEE Trans. Magn. 54 (11) (2018) 2502705.

[69] M.V. Lyange, V.V. Sokolovskiya, S.V. Taskaev, D.Y. Karpenkov, A.V. Bogach, M.V. Zheleznyi, I.V. Shchetinin, V.V. Khovaylo, V.D. Buchelnikov, Effect of disorder on magnetic properties and martensitic transformation of Co-doped Ni-Mn-Al Heusler alloy, Intermetallics 102 (2018) 132–139.

[70] D.E. Soto-Parra, X. Moya, L. Manosa, A. Planes, H. Flores-Zuniga, F. Alvarado-Hernandez, R.A. Ochoa-Gamboa, J.A. Matutes-Aquino, D. Rios-Jara, Fe and Co selective substitution in Ni2MnGa: Effect of magnetism on relative phase stability, Philos. Mag. 90 (20) (2010) 2771–2792.

[71] X.B. Ren, K. Otsuka, Why Does the Martensitic Transformation Temperature Strongly Depend on Composition? Mater. Sci. Forum 327-328 (2000) 429–432.

[72] C.R. Krenn, D. Roundy, J.W. Morris, M.L. Cohen, Ideal strengths of bcc metals, Materials Science and Engineering: A 319-321 (2001) 111–114.

[73] D. Roundy, C.R. Krenn, M.L. Cohen, J.W. Morris, The ideal strength of tungsten, Philos. Mag. A 81 (7) (2001) 1725–1747.

[74] D.M. Clatterbuck, D.C. Chrzan, J.W. Morris, The inherent tensile strength of iron, Philos. Mag. Lett. 82 (3) (2002) 141–147.

[75] E. Orowan, Fracture and strength of solids, Rep. Prog. Phys. 12 (1) (1949) 185–232.

[76] T. Li, J.W. Morris, N. Nagasako, S. Kuramoto, D.C. Chrzan, Ideal" engineering alloys, Phys. Rev. Lett. 98 (10) (2007) 105503.

[77] W. Luo, D. Roundy, M.L. Cohen, J.W. Morris, Ideal strength of bcc molybdenum and niobium, Phys Rev B 66 (9) (2002) 094110.

[78] L. Qi, D.C. Chrzan, Tuning Ideal Tensile Strengths and Intrinsic Ductility of bcc Refractory Alloys, Phys. Rev. Lett. 112 (11) (2014) 115503.

[79] M. Černý, J. Pokluda, Ideal tensile strength of cubic crystals under superimposed transverse biaxial stresses from first principles, Phys Rev B 82 (17) (2010) 174106.

[80] D.M. Clatterbuck, D.C. Chrzan, J.W. Morris, The ideal strength of iron in tension and shear, Acta Mater 51 (8) (2003) 2271–2283.

[81] D.M. Clatterbuck, D.C. Chrzan, J.W. Morris, The influence of triaxial stress on the ideal tensile strength of iron, Scripta Mater 49 (10) (2003) 1007–1011.

[82] N. Nagasako, R. Asahi, J. Hafner, Ideal tensile and shear strength of a gum metal approximant: Ab initio density functional calculations, Phys Rev B 85 (2) (2012) 024122.